Check for updates

Advanced Optical Materials

ADVANCED OPTICAL MATERIALS
www.advopticalmat.de

RESEARCH ARTICLE OPEN ACCESS

Direct Measurement of the Singlet Lifetime and Photoexcitation Behavior of the Boron Vacancy Center in Hexagonal Boron Nitride

Richard A. Escalante[1,2] | Andrew J. Beling[1,3] | Daniel G. Ang[1] | Niko R. Reed[1,3,4] | Justin J. Welter[1,2] | John W. Blanchard[1] | Cecilia Campos[5] | Edwin Coronel[5] | Klaus Krambrock[6] | Alexandre S. Leal[7] | Paras N. Prasad[5] | Ronald L. Walsworth[1,2,3,4]

[1]Quantum Technology Center, University of Maryland, College Park, Maryland, USA | [2]Department of Electrical and Computer Engineering, University of Maryland, College Park, Maryland, USA | [3]Department of Physics, University of Maryland, College Park, Maryland, USA | [4]Joint Quantum Institute, University of Maryland, College Park, Maryland, USA | [5]Institute for Lasers, Photonics and Biophotonics, and the Department of Chemistry, University at Buffalo, State University of New York, Buffalo, New York, USA | [6]Department of Physics, Federal University of Minas Gerais (UFMG), Belo Horizonte, Minas Gerais, Brazil | [7]Nuclear Technology Development Center (CDTN), Belo Horizonte, Minas Gerais, Brazil

Correspondence: Andrew J. Beling (abeling@umd.edu) | Ronald L. Walsworth (walsworth@umd.edu)

Received: 12 April 2026 | **Revised:** 15 May 2026 | **Accepted:** 21 May 2026

Keywords: diamond | hexagonal boron nitride | materials science | nitrogen-vacancy center | photoexcitation | photoluminescence | singlet state | spin states | vacancy defect

ABSTRACT

Optically active spin defects in van der Waals (vdW) materials are a promising platform for quantum sensing, potentially enabling shorter standoff distances than defects in diamond and thus improved measurement signal-to-noise ratio (SNR) and spatial resolution. The most studied such defect is the negatively charged boron vacancy center (V_B^-) in hexagonal boron nitride (hBN), yet many of its electronic and spin transition rates and branching ratios remain unknown. Here, we use time-resolved photoluminescence (PL) measurements with a nanosecond rise-time 515 nm laser to directly measure the singlet state lifetime of a V_B^- ensemble in neutron-irradiated, sub-micron flakes of hBN. We perform this measurement on 16 flakes at room temperature and obtain an average lifetime of 15(3) ns. Additionally, we probe the PL dynamics of thermal and optically polarized electronic spin distributions of the V_B^- ensemble in a sub-micron hBN flake, and fit our results to a 9-level model to extract electronic transition rates. Lastly, we present PL measurements that potentially indicate optically-induced conversion of V_B^- to another electronic state, or possibly the neutral charge state (V_B^0), in neutron-irradiated hBN flakes of size > 1 μm.

1 | Introduction

Research on optically-active spin defects in solid-state materials has grown significantly in recent decades, enabling advances in quantum technologies, including single quantum emitters [1], quantum-based memories [2–4], and quantum sensing [5–8]. The nitrogen vacancy (NV) center in diamond has emerged as the leading solid-state platform in quantum sensing, particularly for magnetometry [7, 9, 10], as well as for electrometry [11], thermometry [12], strain sensing [13], and inertia measurement

Richard A. Escalante and Andrew J. Beling contributed equally to this work.

[Correction added on June 19, 2026, after first online publication: The unit 'micrometers' was corrected to 'microseconds' to reflect the original manuscript specifications. Also, the 12th author has been assigned as corresponding author in this version.]

This is an open access article under the terms of the Creative Commons Attribution License, which permits use, distribution and reproduction in any medium, provided the original work is properly cited.
© 2026 The Author(s). *Advanced Optical Materials* published by Wiley-VCH GmbH

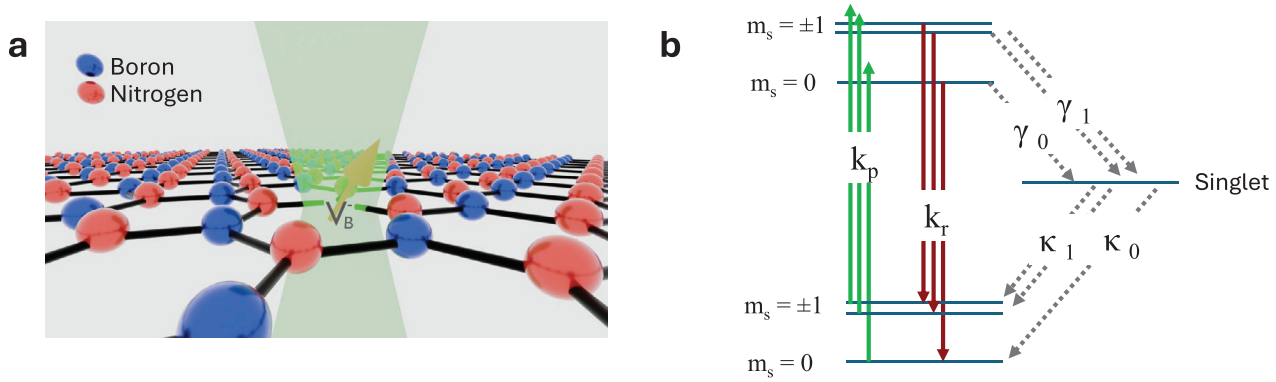


FIGURE 1 | a) Illustration of V_B^- defect in hBN. (b) V_B^- energy level diagram showing the 7-level model.

[14]. However, NVs and other solid-state defects are typically constrained by the need to reside at least several nanometers from the host-material surface, as they become unstable near the material boundary [15]. A defect that remains stable at or near the surface of a two-dimensional (2D) material could substantially reduce the stand-off distance to a given sensing target, potentially providing great value in diverse applications including: nuclear magnetic resonance (NMR) of nanoscale samples [16, 17]; local pressure imaging in diamond anvil cells [18]; and electronic circuit performance evaluation and authenticity validation [19].

Hexagonal boron nitride (hBN) is a van der Waals (vdW) material and promising spin defect host due to its wide band gap, chemical and thermal stability, and optical properties at room temperature. Out of many optically active spin defects within the 2D hBN lattice [20], which can be created by both irradiation and defect center implantation, the negatively charged boron vacancy (V_B^-) (Figure 1a) has attracted interest for sensing due to its similarity to the NV, including a ground state electronic spin triplet with S = 1, optically detected magnetic resonance (ODMR), and optically induced spin polarization, as well as its good optical and spin properties in 3-5 layer flakes of hBN. [21–23] V_B^- ensembles have been used for sensing of magnetic fields, pressure, and temperature, with electronic spin coherence times ~0.1-1 μs [18, 24–28]. Additionally, V_B^- can be easily created in hBN using a variety of irradiation techniques [29–33].

The V_B^- energy level structure is typically approximated by a 7-level model, including ground and excited state spin triplets and a metastable spin singlet state (Figure 1b) [34, 35]. However, despite extensive studies, V_B^- photoexcitation dynamics and properties are not fully understood. In particular, the lifetime of the metastable singlet state (τ_s) has never been directly measured. (In the 7-level model of Figure 1b, the singlet lifetime is given by the inverse of the intersystem crossing rates: $\tau_s = (2\kappa_1 + \kappa_0)^{-1}$.) Previous indirect measurements and theoretical studies report conflicting values (Table 1) [34–38]. For example, Clua-Provost et al. experimentally determined $\tau_s = 18(3)$ ns [34], while Whitefield et al. obtained $\tau_s = 30(1)$ ns [38], and Reimers et al. predicted τ_s = 2 s based on ab initio Density Functional Theory (DFT) calculations [36]. These and other previous experimental studies indirectly extract τ_s from a fit of measured photoluminescence (PL) to an energy level model, switching the incident laser light using standard acousto-optic modulators (AOMs) that have a rise-time significantly longer than the expected $\tau_s \sim 10$–30 ns. [34–38]

TABLE 1 | V_B^- singlet lifetime as reported in prior studies and directly measured in this work. Uncertainties in τ_s measurements are not reported in refs. [35] and [37].

Refs.	τ_s (ns)
Reimers et al., DFT calculation [36]	1.8×10^9
Baber et al., indirect measurement [37]	12.7
Whitefield et al., indirect measurement [38]	30(1)
Clua-Provost et al., indirect measurement [34]	18(3)
Lee et al., indirect measurement [35]	31.5
This work, direct measurement	15(3)
This work, 7-level model	14.4(4)
This work, 9-level model	17.2(6)

A direct measurement of τ_s requires the use of the pulse recovery protocol, with switching of the incident laser light on a timescale fast compared to τ_s, as was previously used to measure the singlet lifetime of the NV center. [39, 40]. Here, we perform a direct measurement of τ_s with the pulse recovery method, utilizing a digitally modulated laser with a fast rise time ($\lesssim$ 2.5 ns, Hubner Cobolt 06-MLD). We perform the measurement on 16 neutron-irradiated, sub-micron-size hBN flakes at room temperature, obtaining a mean value of $\tau_s = 15(3)$ ns.

V_B^- electronic and spin transition rates are also of interest for understanding the spin defect's quantum dynamics; see Figure 1b. Under optical excitation, the transition rate from the ground-state triplet to the excited-state triplet is spin-conserving and given by k_p, which is linearly proportional to the laser power P such that $k_p = Pk_{p_0}$ [34, 38]. The excited state triplet can undergo a spin-conserving radiative decay back to the ground state at rate k_r. It should be noted that excited state lifetime measurements include contributions from both radiative and non-radiative rates, where the non-radiative rates are spin-dependent and denoted by γ_0 and γ_1. Additionally, the first excited state transition is optically forbidden for unstrained hBN, and thus only occurs in the presence of phonons or hBN lattice static distortions (e.g., local strain and other defects); consequently, the quantum efficiency of the V_B^- defect is very low [41, 42]. Ab initio calculations using DFT predict $k_r \approx \frac{1}{11}$ MHz [36] and $k_r \approx \frac{1}{20}$ MHz,[43] which is about 3 orders of magnitude weaker than the NV- radiative decay rate [44].

21951071, 2026, 25, Downloaded from https://advanced.onlinelibrary.wiley.com/doi/10.1002/adom.71351 by Andrew Beling - University Of Maryland , Wiley Online Library on [06/07/2026]. See the Terms and Conditions (https://onlinelibrary.wiley.com/terms-and-conditions) on Wiley Online Library for rules of use; OA articles are governed by the applicable Creative Commons License

Recent measurements using Förster resonance energy transfer (FRET) report $k_r = 0.135$ MHz $\pm$ 0.068 MHz [45], in reasonable agreement with DFT predictions. In ref. [46], k_r is inferred from excited-state lifetime measurements to be equivalent for all 3 spin-states of V_B^-. Like the NV center, the V_B^- center undergoes a spin-dependent non-radiative decay from the excited triplet to a metastable singlet. The excited $m_s = \pm 1$ levels are more likely than the excited $m_s = 0$ level to decay through this pathway, leading to spin-dependent PL brightness. Population in the singlet state decays preferentially to the $m_s = 0$ ground state, causing spin polarization to this brighter PL state, similar to the NV. (See ref. [7] for a thorough discussion of NV spin-dependent PL brightness.)

To determine V_B^- transition rates between energy levels, we perform optical pump-probe measurements of thermal and polarized spin states in a single sub-micron hBN flake, and fit time-resolved PL data to the 7-level model, allowing us to extract the transition rates, κ_0, κ_1, and k_{p0}, as well as the ratio $\frac{\gamma_0}{\gamma_1}$. Nanosecond rise-time laser pulses allow for both direct measurement of the singlet lifetime τ_s and also finer resolution of the sharp PL peak at the beginning of a pulse. The impact of laser rise-time on time-resolved PL is summarized in the Supporting Information. We also study flake- and laser-power-dependent changes to the V_B^- emission spectrum and PL quenching recovery on time scales longer than the measured singlet lifetime. We find that the time-resolved PL data are better represented by a 9-level model of the V_B^- energy structure, with additional laser-power dependent electronic transition rates between the original 7 states and the 2 additional states. Lastly, we report distinct V_B^- photophysical behavior in large hBN flakes (>1 μm), including a long PL decay (~1 μs) for a laser pulse pair with a relatively long wait-time between pulse pair repetition (1 μs), with this long PL decay not observed for laser pulse pairs with a relatively short wait-time (100 ns). Additionally, continuous laser excitation and higher laser powers produce an increase in PL intensity for large hBN flakes within the ~675–775 nm range. This behavior may arise from optically-induced recombination dynamics between defect charge states V_B^- and V_B^0.

2 | Results and Discussion

We investigate the PL behavior of ensembles of V_B^- defects in irradiated hBN flakes at room temperature with a homemade confocal microscope (details in Experimental Methods). Figure 2a shows an example diffraction-limited PL scan of a typical set of flakes. Using a nanosecond rise-time laser with excitation power of approximately 13.6 mW at 515 nm, we identify flakes with a PL emission spectrum like that shown in Figure 2b, with peak emission centered near 825 nm [32]. We report results on smaller hBN flakes (<1 μm) separate from those on larger flakes (>1 μm) because larger flakes exhibit a laser-power dependent change in the PL emission spectrum, possibly indicating photoconversion of V_B^- to other charge states such as V_B^0, which can interfere with the measurement of τ_s (see Figure S2).

2.1 | Singlet Lifetime Measurement

To perform the V_B^- singlet lifetime measurement for an individual sub-micron hBN flake, we apply pairs of closely spaced 515 nm laser excitation pulses and measure the resulting PL time trace (Figure 3a). The pulses are 1 μs long and the spacing between pulses (i.e., dark time t_D) is varied from 0 to 54.8 ns; measurements are enabled by use of the nanosecond rise-time laser. The wait-time between pulse pairs is 100 ns, which we find to be sufficient to allow near-complete population decay to the electronic ground state. This wait-time is chosen based on the experimentally determined singlet lifetime of approximately 18 ns [34], ensuring near-total ground-state population recovery within 100 ns; and is also significantly shorter than the previously measured V_B^- spin-lattice relaxation time T_1 ~13–19 μs [23, 34, 47, 48] and possible recovery dynamics discussed in Sections 2.2 and 2.3, ensuring minimal effect from spin-lattice relaxation and additional relaxation processes during the measurement. For each value of t_D, we repeat the measurement protocol for ~5 min and signal average the results, with an entire set of measurements for all t_D values requiring ~1 h. We observe a clear recovery in PL peak height with increasing t_D, due to excited state population decaying to the ground state before the second pulse (Figure 3b). To extract the metastable singlet state lifetime τ_s, we take the ratio of the (signal-averaged) height of the second PL peak to that of the first peak and plot it as a function of the dark time, t_D (Figure 3c). The measurement is then repeated on 16 hBN sub-micron flakes from the same batch (Figure 3d). Averaging results from all flakes, we obtain a mean $\tau_s = 15(3)$ ns; this value is consistent with Clua-Provost et al.,[34] which indirectly inferred $\tau_s = 18(3)$ ns. The contrast of observed PL peak height to the steady state PL value under laser excitation can give a lower bound estimate on V_B^- polarization to the singlet state [49]. We report this value for the 16 studied sub-micron hBN flakes in Figure S8.

The modest observed variability in τ_s values from the studied set of 16 sub-micron hBN flakes may be a result of differences in flake properties. A prior study [46] observed variations in excitation laser light absorption, PL collection efficiency, and Purcell factor depending on flake thickness and defect depth. Another possibility is variation in the susceptibility of different flakes to optically-induced changes in defect charge state; e.g., if the other charge state is dark (i.e., does not produce observable PL), it would act as an additional shelving state and affect determination of τ_s from PL recovery measurements.

2.2 | Measurements of Transition Rates

To determine the V_B^- energy level transition rates, we measure time-resolved PL from a single sub-micron hBN flake as a function of laser power and initial ground-state spin distribution. We apply pairs of 1 μs laser pulses, with a dark time between pulses of 100 ns and a wait-time between pulse pairs of 100 μs. V_B^- PL is measured during the application of each laser pulse (see measurement sequence in Figure 4a). The wait-time is chosen to be long compared to the V_B^- spin-lattice relaxation time T_1 ~13–19 μs [23, 34, 47, 48], thereby allowing the V_B^- spin population to fully relax to a thermal distribution between each laser pulse pair. The 100 ns dark time between laser pulses is short compared to T_1, but long compared to the measured singlet lifetime τ_s, thereby allowing study of the photophysics of a nearly spin-polarized V_B^- ensemble. The measured photophysical response, i.e., PL dynamics, of the thermal and polarized V_B^-

21951071, 2026, 25, Downloaded from https://advanced.onlinelibrary.wiley.com/doi/10.1002/adom.71351 by Andrew Beling - University Of Maryland , Wiley Online Library on [06/07/2026]. See the Terms and Conditions (https://onlinelibrary.wiley.com/terms-and-conditions) on Wiley Online Library for rules of use; OA articles are governed by the applicable Creative Commons License

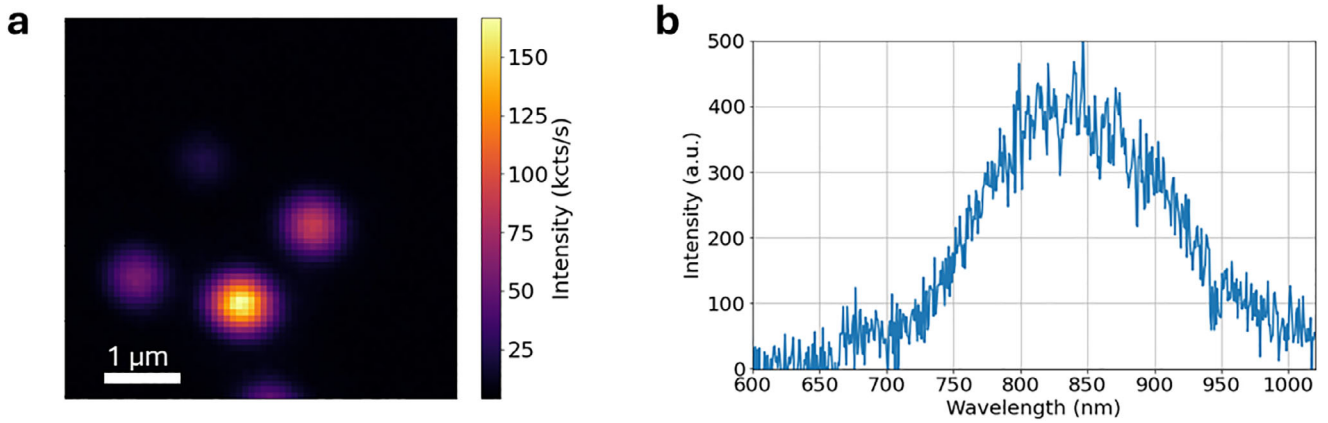


FIGURE 2 | (a) Example scanned-confocal PL map of neutron irradiated flakes of hBN. (b) Typical V_B^- PL emission spectrum for a sub-micron hBN flake with peak emission centered near 825 nm.

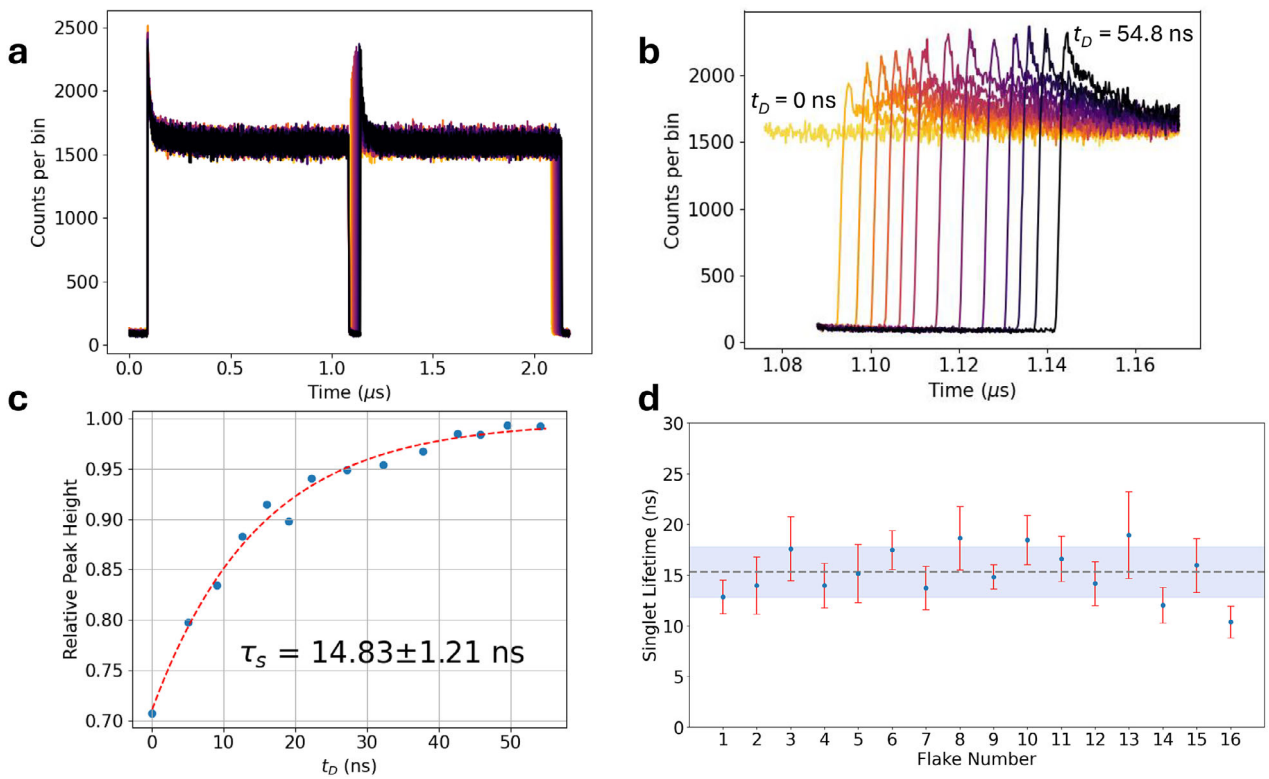


FIGURE 3 | (a) Example signal-averaged PL time traces from a sub-micron hBN flake induced by pairs of 1 μs laser pulses, with spacings between pulses (dark time t_D) ranging from 0 ns to 54.8 ns. (b) Zoomed-in display of PL time-trace data in a) from the second laser pulse showing PL peak height recovery for different t_D. (c) Measured relative PL peak height as a function of t_D for one sub-micron hBN flake. Red dashed curve shows exponential fit yielding metastable singlet state lifetime τ_s for this flake. (d) Fitted τ_s values and uncertainties from PL time-trace measurements of 16 sub-micron hBN flakes. Gray dashed line designates mean lifetime from all the flakes and shaded region is standard deviation: $\tau_s = 15(3)$ ns.

electron spin distributions are shown in Figure 5a. We repeat the measurements for five laser powers between 3.71 and 21.3 mW (measured at the focus of the beam after the objective). Signal-averaged PL from the first ~200 ns of each laser pulse is shown in Figure 5a, with full PL data given in the Supporting Information. For both V_B^- distributions, there is an initial PL peak followed by PL quenching and equilibration to a steady-state value, resulting from rapid optical initialization to the photoluminescent excited states and then partial population decay to the dark singlet state. For the thermal distribution, PL recovers from a minimum to a steady-state value as spin population is polarized to the relatively brighter $m_s = 0$ state. Optical initialization to $m_s = 0$ occurs faster for higher laser powers, with steady-state PL achieved within ~100–300 ns. The exception to this behavior is at the highest power (21.3 mW), where a decay in counts occurs on longer time scales (Figure S5).

21951071, 2026, 25, Downloaded from https://advanced.onlinelibrary.wiley.com/doi/10.1002/adom.71351 by Andrew Beling - University Of Maryland , Wiley Online Library on [06/07/2026]. See the Terms and Conditions (https://onlinelibrary.wiley.com/terms-and-conditions) on Wiley Online Library for rules of use; OA articles are governed by the applicable Creative Commons License

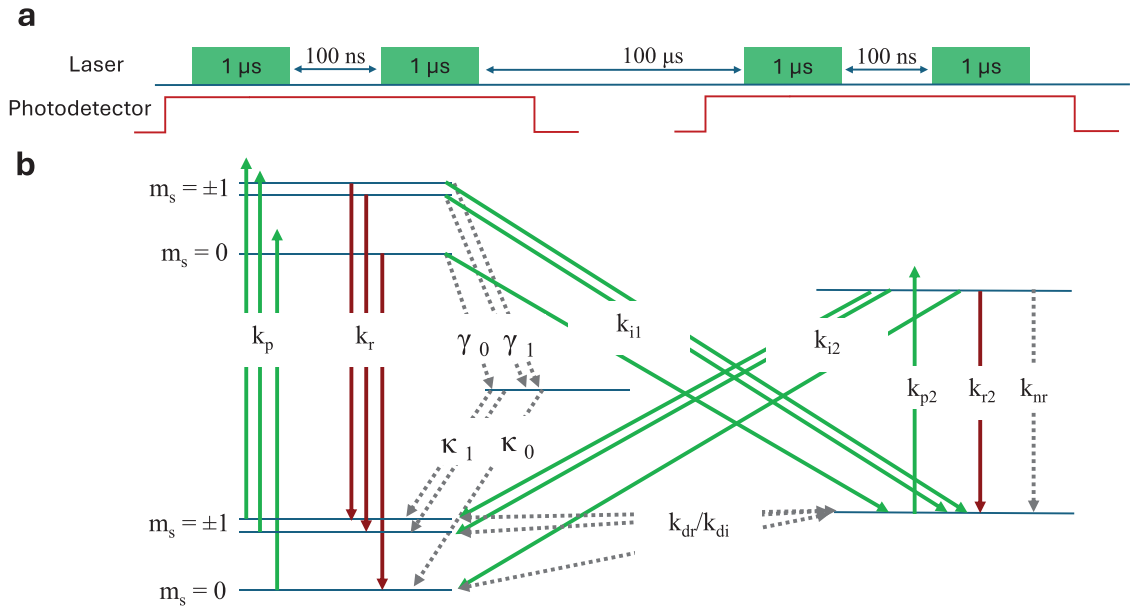


FIGURE 4 | (a) Measurement sequence used to probe PL from the thermal and polarized electronic spin distributions of ensembles of V_B^- in a neutron irradiated flake of hBN. A pair of 1 μs laser pulses is applied with a dark time spacing of 100 ns. The 1 μs pulse duration allows partial spin polarization to the singlet state. The 100 ns dark time is sufficient for significant decay from the singlet state, preferentially to the $m_s = 0$ ground state (see Figure 1b), at which point the second laser pulse induces PL from the polarized spin distribution. The 100 μs wait-time between pulse pairs is significantly longer than the V_B^- spin T_1 to allow for full depolarization to a thermal spin distribution. (b) Modified V_B^- energy level diagram (9-level model) including 2 additional states to better describe thermal and polarized spin distribution PL data. Additional conversion pathways between the 2 additional states and the ground and singlet states of the 7-level model do not measurably influence fits to data and are thus are omitted.

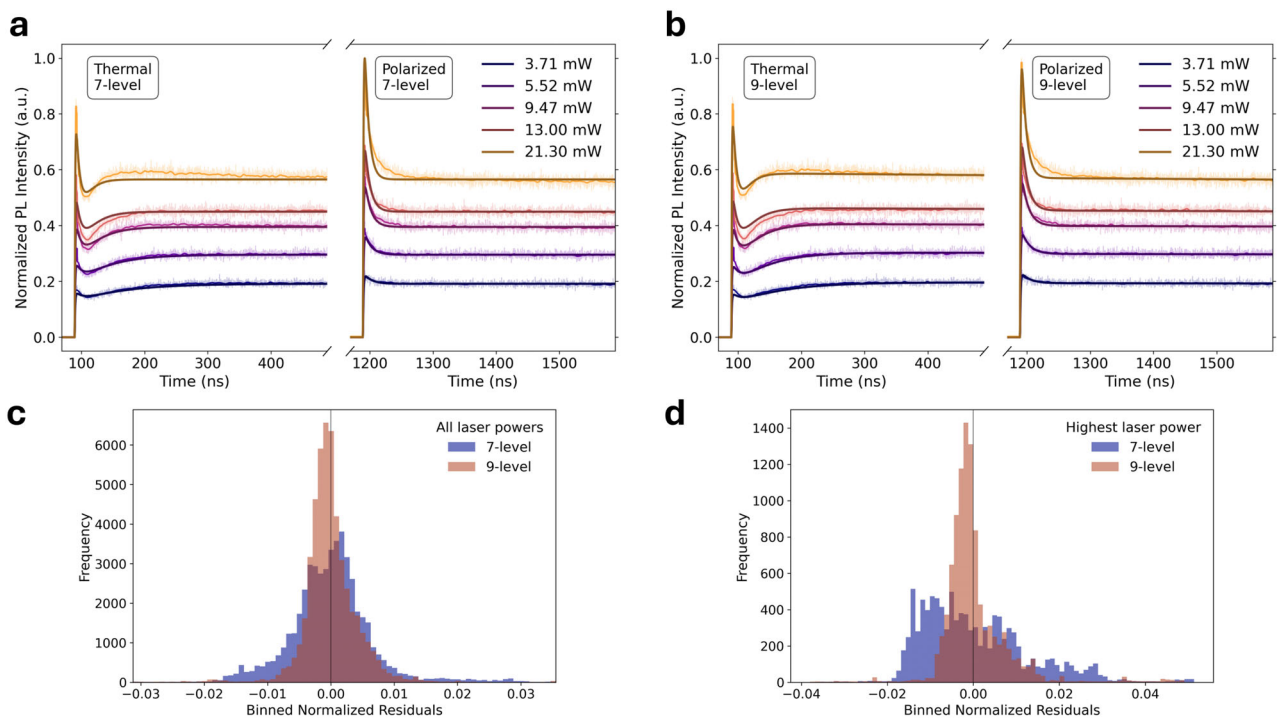


FIGURE 5 | (a, b) Measured PL time traces for a sub-micron hBN flake at room temperature, following the sequence in Figure 4a), showing thermal (left) and polarized (right) V_B^- spin distributions and fits to the (a) 7-level model, (b) 9-level model. For each laser power, PL measurements are repeated and signal averaged over ~15 min, with an entire set of measurements for all laser powers requiring ~ 1.5 h. Raw data is smoothed with a mean shift filter and shown with a semi-opaque color scale compared to the smoothed data and fits (solid lines). (c) Histograms of fit residuals for all five laser powers, comparing the 7-level and 9-level model fits to the data. The distribution of 9-level model residuals is more sharply peaked around 0, indicating a better fit. d) Histograms of fit residuals for the highest laser power. The distribution of 7-level model residuals has a wider spread compared to (c); whereas the distribution of 9-level model residuals remains sharply peaked around 0.

21951071, 2026, 25, Downloaded from https://advanced.onlinelibrary.wiley.com/doi/10.1002/adom.71351 by Andrew Beling - University Of Maryland , Wiley Online Library on [06/07/2026]. See the Terms and Conditions (https://onlinelibrary.wiley.com/terms-and-conditions) on Wiley Online Library for rules of use; OA articles are governed by the applicable Creative Commons License

TABLE 2 | Boron vacancy electronic transition rates from the 7-level model fit to time-resolved PL data from a single sub-micron hBN flake (details of fit presented in the Supporting Information) and from previous papers.

Refs.	k_{p_0} (MHz/mW)	k_r (MHz)	γ_0 (MHz)	γ_1 (MHz)	κ_0 (MHz)	κ_1 (MHz)
This work, 7-level model	3.6(1)	0.091 from ref. [36]	1.003×10^3 (fixed)	$2.14(1) \times 10^3$	58(1)	5.8(2)
Baber et al. [37]	Not stated	0.091 from ref. [36]	1.01×10^3	2.03×10^3	20	29.4
Whitefield et al. [38]	Not stated	$8.8(3) \times 10^2$	$1.3(3) \times 10^2$	$1.15(3) \times 10^3$	13(1)	10(1)
Clua-Provost et al. [34]	1.0(4)	0.091 from ref. [36]	$8.2(6) \times 10^2$	$1.8(2) \times 10^3$	41(8)	7(2)
Lee et al. [35]	Not stated	8.49×10^2	< 51.44	1.286×10^3	22.7	4.54

For both thermal and polarized spin distribution measurements, we first fit the time-resolved PL data to the 7-level model of the V_B^- electronic and spin energy levels (see Figure 1b). To bound the parameters more reliably and reduce sensitivity to local minima, we use a multi-start fitting routine based on Latin hypercube sampling (LHS) of the parameter space (see refs. [50] and [51]). We keep k_{p0}, κ_0, κ_1, and the ratio between non-radiative decay-rates $\frac{\gamma_0}{\gamma_1}$ as free parameters in the model and set the radiative decay rate k_r to the DFT simulation value [36]. k_{p_0} is a fit parameter that determines the scaling of the optical pumping rate k_p with laser power, P, such that $k_p = P \cdot k_{p_0}$. The LHS fitting procedure indicates that the absolute magnitudes of γ_0 and γ_1 are not uniquely constrained by the PL data, whereas the ratio $\frac{\gamma_0}{\gamma_1}$ converges robustly; therefore, either γ_0 or γ_1 must be constrained by an independent measurement. Hence, we fix γ_0 determined from a literature average of directly measured $m_s = 0$ excited state lifetimes (τ_0) [34, 35, 37]. Using $\tau_0 = \frac{1}{k_r + \gamma_0}$ and $k_r << \gamma_0$ [34, 36, 43, 45], yields $\gamma_0 = 1/\tau_0$. Fit parameter uncertainties are calculated by adding in quadrature the statistical uncertainty of the fit, obtained from bootstrap resampling of the data, and the systematic uncertainty estimated from jackknife resampling [52] of data at different laser powers. Details of PL data fitting to the 7-level model are given in the Supporting Information, with resulting transition rates summarized in Table 2 and compared to past results.

The fit results demonstrate that the 7-level model accurately accounts for normalized PL measurements at low laser powers. From the reverse intersystem crossing rates κ_0 and κ_1, we extract the singlet lifetime $\tau_s = \frac{1}{\kappa_0 + 2\kappa_1} = 14.4(4)$ ns, which is consistent with our independent measurement of τ_s in Section 2.1. However, the 7-level model fails to give good fits to data at high laser powers. At the highest laser power (21.3 mW), the model does not account for the observed long-time PL quenching (decay) over the course of the first laser pulse (Figure 5 and Figure S5).

To achieve a better fit including PL quenching behavior at high laser powers, we utilize a 9-level model that introduces coupling to an additional 2-level system (Figure 4b). The 9-level model incorporates optical pumping (k_{p2}), radiative decay (k_{r2}), and non-radiative decay (k_{nr}) between the two additional levels, as well as transition rates between the 7- and 2-level manifolds through dark conversion (k_{di}), dark recombination (k_{dr}), photo-conversion (k_{i1}), and photorecombination (k_{i2}). Similar to k_{p_0}, k_{p2_0}, k_{i1_0}, and k_{i2_0} are fit parameters that determine the scaling of the k_{p2}, k_{i1}, and k_{i2} rates with laser power, respectively. The exact laser power dependencies are defined in the Supporting Information. As with the 7-level model, we fix γ_0 to a literature average of directly measured $m_s = 0$ lifetimes and leave the ratio γ_0/γ_1 free [34, 35, 37]. We base this modified 9-level energy structure and additional transition rates on prior work that models NV charge-state photoexcitation dynamics [44, 53], wherein the NV^0 charge-state is modeled as a 2-level system connected to a 7-level NV^- charge-state manifold.

Fits of time-resolved PL data to the 9-level model represent observed behavior better than fits to the 7-level model (Figure 5a vs. Figure 5b). In particular, the 9-level model replicates the observed PL quenching for the highest laser power. Quantitatively, the sum of squared residuals (SSRs) for the total dataset is lower for the 9-level model (2.13) compared to the 7-level model (3.44), demonstrating a $\sim 60\%$ better fit to the data. The improved fit quality is more drastic for the highest laser power of 21.3 mW, where SSRs are more than twice as small for the 9-level model compared to the 7-level model. Figure 5c,d shows a histogram of fit residuals between the data and each model for all 5 laser powers and for the highest laser power only, respectively. In both cases, fit residuals are more sharply peaked around 0 for the 9-level model, indicating an improved fit quality, especially for the highest laser power.

Table 3 summarizes transition rates determined from 9-level model fits to PL measurements for both polarized and thermal V_B^- spin distributions at several laser powers, again setting k_r to the DFT simulation value [36]. Fit parameters k_{dr} and k_{i2_0} are found to be very small and do not materially influence the fit when left as free parameters, and thus are set to zero. We note that a non-zero recombination pathway, represented by fit parameters k_{dr} and k_{i2_0}, from the 2 level system to the 7 level system is required to sustain a finite V_B^- population in the steady-state; however, the sensitivity of our model and data is insufficient to place meaningful bounds on these recombination rates. Fit parameter uncertainties are calculated following the same procedure as for the 7-level model, with an additional model-dependent contribution defined as the difference in fitted parameter values between the quadratic-k_{i1} and linear-k_{i1} models, with the former providing a modestly better fit, as described below. Details of the fitting and uncertainty analysis are given in the Supporting Information.

Further work is needed to understand the physical origin of the additional 2 levels in the 9-level model, e.g., whether they are related to a different boron vacancy charge state, such as V_B^0. We note that modestly improved fits to PL time-course data are achieved for a quadratic laser-power dependence of photoconversion (k_{i1}) from the original 7-level excited states

21951071, 2026, 25, Downloaded from https://advanced.onlinelibrary.wiley.com/doi/10.1002/adom.71351 by Andrew Beling - University Of Maryland , Wiley Online Library on [06/07/2026]. See the Terms and Conditions (https://onlinelibrary.wiley.com/terms-and-conditions) on Wiley Online Library for rules of use; OA articles are governed by the applicable Creative Commons License

TABLE 3 | Boron vacancy electronic transition rates from the 9-level model fit to time-resolved PL data from a single sub-micron hBN flake (see fits and data in Figure 5b). Details on the fitting procedure are given in the Supporting Information.

Electronic transition rate	9-Level model fit
k_{p0} (MHz/mW)	3.5(2)
k_r (MHz)	0.091 (DFT) from ref. [36]
γ_0 (MHz)	1.003×10^3 (fixed)
γ_1 (MHz)	$2.19(3) \times 10^3$
κ_0 (MHz)	56.0(8)
κ_1 (MHz)	< 2
k_{p2_0} (MHz/mW)	84(11)
k_{i1_0} (MHz/mW^2)	$1.72(3) \times 10^{-2}$
k_{i2_0} (MHz/mW)	0 (fixed)
k_{r2} (MHz)	$4.5(3) \times 10^{-3}$
k_{nr} (MHz)	$1.5(2) \times 10^3$
k_{di} (MHz)	0.15(6)
k_{dr} (MHz)	0 (fixed)

to the additional 2-level manifold. Motivated by established NV photoionization dynamics [44, 54–56], we incorporate into the rate equation fit three possible photoconversion pathways from the ground, singlet, and excited states to the two-level manifold. Only the excited state pathway results in a non-zero photoconversion fit parameter that improves fit quality. The fitted rates of the other two pathways converge to values several orders of magnitude smaller than the excited-state photoconversion rate, and do not change fit quality when set to 0. Therefore, we fix these rates to zero in the final fit. Charge transition level calculations suggest V_B^0 can possibly be converted to V_B^- and vice versa under photo-excitation with 515 nm illumination [57, 58]. However, recent theory work has emphasized that such ab initio charge-transition thresholds can carry substantial uncertainty and should be treated as semi-quantitative indicators rather than precise predictions [59]. Accordingly, although the additional two levels in our 9-level description are consistent with the measured PL dynamics, we regard them only as a heuristic model. Detailed understanding of the pathways, dynamics, laser-intensity dependence, and wavelength dependence of V_B^- photoconversion are important open questions for future experimental study.

2.3 | PL Spectral Behavior and Dynamics for Larger hBN Flakes (>1 μm)

We observe distinctly different photophysical behavior in neutron-irradiated hBN flakes with size greater than ∼1 μm. Figure 6a shows a PL confocal scan of one such large flake. We characterize the PL behavior of a single large hBN flake by applying two different laser pulse-pair sequences, with 1 μs pulse time, dark time $t_D = 5$ ns between pulses, and wait-times between pulse pairs of either 100 ns or 1 μs. We perform time-resolved PL measurements using these pulse-pair sequences, while also monitoring the PL emission spectrum. The resulting PL time traces (signal averaged over ∼5 min for each wait-time sequence) are shown in Figure 6b. For the 1 μs wait-time, we observe a long PL decay (∼1 μs) that is not observed for the 100 ns wait-time. Full PL recovery after this long decay is on the order of several hundreds of ns.

For continuous laser excitation and the 100 ns pulse pair wait-time sequence, we observe an increase in PL emission as a function of laser power in the range of ∼675–775 nm, when compared to measurements for the 1 μs pulse pair wait-time sequence (see Figure 6c,d). Each of these measurements are performed using a broadband optical spectrometer with about 1 min of signal averaging. This behavior contrasts with that observed in sub-micron hBN flakes, for which no significant laser-power dependence is observed in the normalized PL emission spectrum (see Figure S3). Our working hypothesis to explain these observations is that a laser-power dependent increase in PL ∼675–775 nm in larger hBN flakes arises from enhanced conversion of V_B^- to V_B^0 (or perhaps another charge state) under continuous laser excitation and the 100 ns pulse pair wait-time sequence; whereas for the 1 μs wait-time sequence in larger hBN flakes — and also for sub-micron flakes under any of the laser excitation protocols — there is sufficient time for charge-state recombination back to V_B^-, and hence no enhanced PL ∼675–775 nm. This phenomenon requires further investigations to fully understand the underlying mechanisms, which could arise from strain, aggregates of smaller hBN flakes, or edge effects, e.g., measurements of PL behavior as a function of temperature and laser wavelength, as well as hBN flake size and defect/material preparation.

3 | Conclusion

In summary, we employ a nanosecond rise-time 515 nm laser to perform a direct measurement of the singlet lifetime of an ensemble of V_B^- (boron vacancy) defects in neutron-irradiated, sub-micron flakes of hBN. We repeat the measurement on 16 hBN flakes at room temperature and obtain a mean lifetime $\tau_s = 15(3)$ ns. For a single sub-micron hBN flake, we measure photoluminescence (PL) time traces for thermal and polarized electronic spin distributions of the boron vacancy ensemble. Fitting the PL time-course data to a 9-level model of V_B^- electronic and spin levels, we extract more accurate values for the electronic energy level transition rates than for the conventional 7-level model, potentially indicating optically-induced conversion to V_B^0 or another state. We also observe distinct PL behavior in large (>1 μm) neutron-irradiated hBN flakes that may result from optically-induced changes in boron vacancy charge state. This behavior includes a long (∼1 μs) PL decay for an extended wait-time (∼1 μs) between laser pulse-pairs; and an increase in PL emission as a function of excitation laser power in the range ∼675–775 nm for continuous laser excitation or for a short (100 ns) wait-time between laser pulse-pairs. These measurements add to the growing understanding of the V_B^- defect in hBN.

4 | Experimental Methods

4.1 | Sample Preparation

hBN samples (micro-powder from 2D Semiconductors, USA) are neutron-irradiated in a Triga Mark IPR-R1 nuclear reactor

21951071, 2026, 25, Downloaded from https://advanced.onlinelibrary.wiley.com/doi/10.1002/adom.71351 by Andrew Beling - University Of Maryland , Wiley Online Library on [06/07/2026]. See the Terms and Conditions (https://onlinelibrary.wiley.com/terms-and-conditions) on Wiley Online Library for rules of use; OA articles are governed by the applicable Creative Commons License

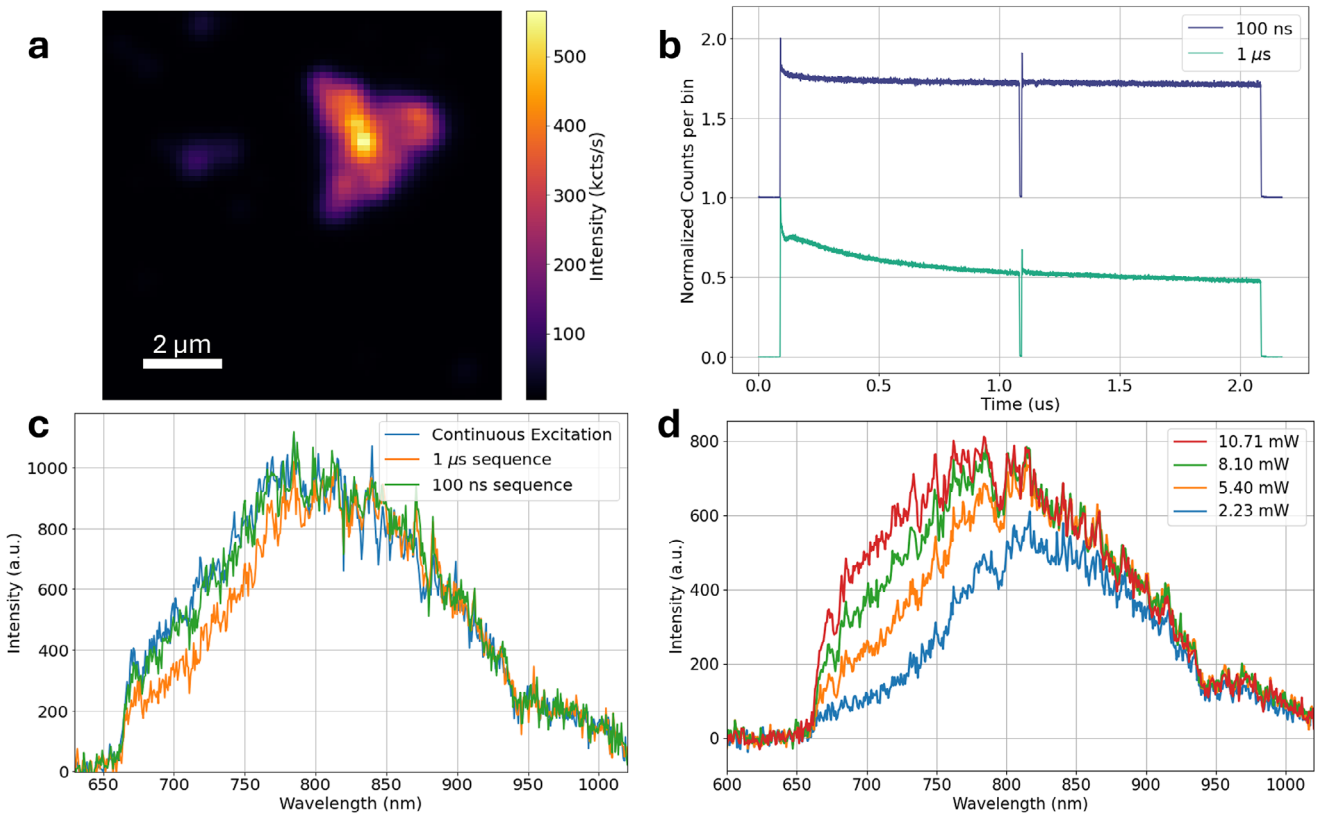


FIGURE 6 | (a) Example confocal PL map of a large (>1 μm) flake of neutron irradiated hBN. These larger flakes display different PL behavior from sub-micron flakes. (b) Time-resolved PL measurements from a single large hBN flake for laser pulse pairs with 1 μs pulse time and dark time $t_D = 5$ ns between pulses. The top set of signal-averaged PL measurements has a wait-time of 100 ns between pulse pairs while the lower has a 1 μs wait-time. The long decay (~1 μs) observed during the first pulse of the 1 μs wait-time sequence may result from partial conversion of V_B^- to V_B^0 within the ensemble of defects. (c) PL emission spectra for continuous laser excitation, the 1 μs pulse pair wait-time sequence, and the 100 ns pulse pair wait-time sequence, with all measurements performed using 11.6 mW laser power. Note the observed increase in PL in the ~675–775 nm range for continuous excitation and the 100 ns pulse pair wait-time sequence, potentially due to enhanced conversion of V_B^- to V_B^0. This increase is not observed for the 1 μs sequence, potentially because this longer pulse pair wait-time is sufficient for recombination back to V_B^-. (d) PL emission spectra of a large hBN flake for 4 laser excitation powers. In both (c) and (d), the sharp cut-off observed at ~660 nm is from the dichroic mirror (Thorlabs DMLP650R).

(CDTN, Brazil), with thermal neutron flux of 4×10^{12} n cm^{-2} s^{-1} up to a total dose of 2.3×10^{17} n cm^{-2} (16 h). Considering that thermal neutrons are blocked by a Cd capsule, and the fast and epithermal neutron flux is about one order of magnitude lower, the total neutron dose to the hBN samples is about 2.3×10^{16} n cm^{-2}. Compared to electron, proton, and ion irradiations, fast neutrons have no electrical charge, and therefore present homogeneous and high penetration depths in almost all materials [60]. Irradiated hBN samples are pre-characterized by electron paramagnetic resonance (EPR) in the 10 to 300 K temperature range, from which the presence of V_B^- defects is inferred [61]. Irradiated samples, consisting of flakes up to 5 μm in size, are sonicated in solution and dropcast on a glass cover slip.

4.2 | Photoluminescence (PL) Measurement Setup

Measurements are performed using a home-built confocal microscope with a digitally modulated fast rise-time 515 nm laser (Hübner Cobolt 06-MLD). To control the laser modulation, we use a Pulse Streamer 8/2 (Swabian Instruments) along with a TTL buffer (Texas Instrument SN64BCT25244DW) to raise the pulse signal from 2.6 to 5 V, which is the optimal voltage to drive the Cobolt 06-MLD. To excite boron vacancy photoluminescence (PL) from an hBN sample, a dichroic mirror (Thorlabs DMLP650R) is used to steer the incident laser beam to an infrared objective (0.7 NA OptoSigma PAL-100-NIR-HR). PL is focused through a pinhole and split with a 50-50 beam splitter (Thorlabs CCM1-BS014). All mirrors after the pinhole are broadband dielectric mirrors (Thorlabs BB1-E03-10). One path is filtered using a 700 nm long pass (Thorlabs FEL0700) and a 900 nm short pass (Thorlabs FESH0900) and coupled via a fiber to a photodetector (Excelitas SPCM-AQRH-W5-FC). The other path is filtered with a 550 nm long pass and directed to a spectrometer (Ocean Optics QE Pro). Time-resolved PL measurements are performed using a Swabian Time Tagger 20 to record pulses from the photodetector.

Acknowledgements

We thank Alessandro Restelli for technical assistance regarding electronics in the experiment; and Sean Blakley and Kristine Ung for helpful discussions. K. Krambrock thanks the Brazilian agencies CNPq and Fapemig for financial support. This work is supported by, or in part by, the U.S. Air Force Office of Scientific Research under Grant No.

21951071, 2026, 25, Downloaded from https://advanced.onlinelibrary.wiley.com/doi/10.1002/adom.71351 by Andrew Beling - University Of Maryland , Wiley Online Library on [06/07/2026]. See the Terms and Conditions (https://onlinelibrary.wiley.com/terms-and-conditions) on Wiley Online Library for rules of use; OA articles are governed by the applicable Creative Commons License

FA9550-22-1-0312 as part of the MURI project Comprehensive Minimally/non-invasive Multifaceted Assessment of Nano-/microelectronic Devices (CoMMAND); the National Science Foundation Graduate Research Fellowship Program under Grant No. DGE 2236417; the Laboratory for Physical Sciences Jumping Electron Quantum Fellowship Program under Award No. H9823022C0029; the U.S. Army Research Laboratory under Contract No. W911NF2420143; the Maryland Procurement Office under Award No. H9823019C0220; and the University of Maryland Quantum Technology Center.

Conflicts of Interest

The authors declare no conflicts of interest.

Data Availability Statement

The data that support the findings of this study are available from the corresponding author upon reasonable request.

References

1. I. Aharonovich, D. Englund, and M. Toth, "Solid-State Single-Photon Emitters," *Nature Photonics* 10, no. 10 (2016): 631–641.

2. C. E. Bradley, S. W. de Bone, P. F. W. Möller, et al., "Robust Quantum-Network Memory Based on Spin Qubits in Isotopically Engineered Diamond," *npj Quantum Information* 8, no. 1 (2022): 122.

3. D. Sukachev, A. Sipahigil, C. Nguyen, et al., "Silicon-Vacancy Spin Qubit in Diamond: A Quantum Memory Exceeding 10 ms with Single-Shot State Readout," *Physical Review Letters* 119, no. 22 (2017): 223602.

4. S. K. Parthasarathy, B. Kallinger, F. Kaiser, et al., "Scalable Quantum Memory Nodes Using Nuclear Spins in Silicon Carbide," *Physical Review Applied* 19, no. 3 (2023): 034026.

5. J. R. Maze, P. L. Stanwix, J. S. Hodges, et al., "Nanoscale Magnetic Sensing with an Individual Electronic Spin in Diamond," *Nature* 455, no. 7213 (2008): 644–647.

6. S. Hsieh, P. Bhattacharyya, C. Zu, et al., "Imaging Stress and Magnetism at High Pressures Using a Nanoscale Quantum Sensor," *Science* 366, no. 6471 (2019): 1349–1354.

7. J. F. Barry, J. M. Schloss, E. Bauch, et al., "Sensitivity Optimization for NV-Diamond Magnetometry," *Reviews of Modern Physics* 92, no. 1 (2020): 015004.

8. J.-F. Wang, L. Liu, X.-D. Liu, et al., "Magnetic Detection under High Pressures Using Designed Silicon Vacancy Centres in Silicon Carbide," *Nature Materials* 22, no. 4 (2023): 489–494.

9. L. Rondin, J.-P. Tetienne, T. Hingant, J.-F. Roch, P. Maletinsky, and V. Jacques, "Magnetometry with Nitrogen-Vacancy Defects in Diamond," *Reports on Progress in Physics* 77, no. 5 (2014): 056503.

10. N. Sekiguchi, M. Fushimi, A. Yoshimura, et al., "Diamond Quantum Magnetometer with dc Sensitivity of Sub-10 pT $Hz^{-1/2}$ toward Measurement of Biomagnetic Field," *Physical Review Applied* 21, no. 6 (2024): 064010.

11. K. Bian, W. Zheng, X. Zeng, et al., "Nanoscale Electric-Field Imaging Based on a Quantum Sensor and Its Charge-State Control under Ambient Condition," *Nature Communications* 12, no. 1 (2021): 2457.

12. J. Wang, F. Feng, J. Zhang, et al., "High-Sensitivity Temperature Sensing Using an Implanted Single Nitrogen-Vacancy Center Array in Diamond," *Physical Review B* 91, no. 15 (2015): 155404.

13. M. C. Marshall, R. Ebadi, C. Hart, et al., "High-Precision Mapping of Diamond Crystal Strain Using Quantum Interferometry," *Physical Review Applied* 17, no. 2 (2022): 024041.

14. L. Zhao, X. Shen, L. Ji, and P. Huang, "Inertial Measurement with Solid-State Spins of Nitrogen-Vacancy Center in Diamond," *Advances in Physics: X* 7, no. 1 (2022): 2004921.

15. R. Kumar, S. Mahajan, F. Donaldson, et al., "Stability of Near-Surface Nitrogen Vacancy Centers Using Dielectric Surface Passivation," *ACS Photonics* 11, no. 3 (2024): 1244–1251.

16. D. M. Daly, N. R. Reed, S. J. DeVience, et al., "Prospects for Ultralow-Mass Nuclear Magnetic Resonance Using Spin Defects in Hexagonal Boron Nitride," 2025, https://arxiv.org/abs/2505.00383.

17. S. Vaidya, X. Gao, S. Dikshit, I. Aharonovich, and T. Li, "Quantum Sensing and Imaging with Spin Defects in Hexagonal Boron Nitride," *Advances in Physics: X* 8, no. 1 (2023): 2206049.

18. G. He, R. Gong, Z. Wang, et al., "Probing Stress and Magnetism at High Pressures with Two-Dimensional Quantum Sensors," 2025. http://arxiv.org/abs/2501.03319.

19. M. Ashok, M. J. Turner, R. L. Walsworth, E. V. Levine, and A. P. Chandrakasan, "Hardware Trojan Detection Using Unsupervised Deep Learning on Quantum Diamond Microscope Magnetic Field Images," *ACM Journal on Emerging Technologies in Computing Systems* 18, no. 4 (2022): 1–25.

20. E. Glushkov, M. Macha, E. Räth, et al., "Engineering Optically Active Defects in Hexagonal Boron Nitride Using Focused Ion Beam and Water," *ACS Nano* 16, no. 3 (2022): 3695.

21. N. Mathur, A. Mukherjee, X. Gao, et al., "Excited-State Spin-Resonance Spectroscopy of V_B^- Defect Centers in Hexagonal Boron Nitride," *Nature Communications* 13, no. 1 (2022): 3233.

22. N.-J. Guo, W. Liu, Z.-P. Li, et al., "Generation of Spin Defects by Ion Implantation in Hexagonal Boron Nitride," *ACS Omega* 7, no. 2 (2022): 1733–1739.

23. A. Durand, T. Clua-Provost, F. Fabre, et al., "Optically Active Spin Defects in Few-Layer Thick Hexagonal Boron Nitride," *Physical Review Letters* 131 (2023): 116902.

24. W. Liu, Z.-P. Li, Y.-Z. Yang, et al., "Temperature-Dependent Energy-Level Shifts of Spin Defects in Hexagonal Boron Nitride," *ACS Photonics* 8, no. 7 (2021): 1889.

25. A. J. Healey, S. C. Scholten, T. Yang, et al., "Quantum Microscopy with van der Waals Heterostructures," *Nature Physics* 19, no. 1 (2023): 87.

26. Z. Mu, J. Fraunié, A. Durand, et al., "Magnetic Imaging under High Pressure with a Spin-Based Quantum Sensor Integrated in a van der Waals Heterostructure," 2025, http://arxiv.org/abs/2501.03640.

27. A. Gottscholl, M. Diez, V. Soltamov, et al., "Spin Defects in hBN as Promising Temperature, Pressure and Magnetic Field Quantum Sensors," *Nature Communications* 12, no. 1 (2021): 4480.

28. X. Gao, B. Jiang, A. E. Llacsahuanga Allcca, et al., "High-Contrast Plasmonic-Enhanced Shallow Spin Defects in Hexagonal Boron Nitride for Quantum Sensing," *Nano Letters* 21, no. 18 (2021): 7708.

29. M. Kianinia, S. White, J. E. Fröch, C. Bradac, and I. Aharonovich, "Generation of Spin Defects in Hexagonal Boron Nitride," *ACS Photonics* 7, no. 8 (2020): 2147.

30. X. Gao, S. Pandey, M. Kianinia, et al., "Femtosecond Laser Writing of Spin Defects in Hexagonal Boron Nitride," *ACS Photonics* 8, no. 4 (2021): 994–1000.

31. F. Murzakhanov, B. Yavkin, G. Mamin, et al., "Creation of Negatively Charged Boron Vacancies in Hexagonal Boron Nitride Crystal by Electron Irradiation and Mechanism of Inhomogeneous Broadening of Boron Vacancy-Related Spin Resonance Lines," *Nanomaterials* 11, no. 6 (2021): 1373.

32. A. Gottscholl, M. Kianinia, V. Soltamov, et al., "Initialization and Read-Out of Intrinsic Spin Defects in a van der Waals Crystal at Room Temperature," *Nature Materials* 19, no. 5 (2020): 540–545.

33. J. R. Toledo, D. B. de Jesus, M. Kianinia, et al., "Electron Paramagnetic Resonance Signature of Point Defects in Neutron-Irradiated Hexagonal Boron Nitride," *Physical Review B* 98, no. 15 (2018): 155203.

21951071, 2026, 25, Downloaded from https://advanced.onlinelibrary.wiley.com/doi/10.1002/adom.71351 by Andrew Beling - University Of Maryland , Wiley Online Library on [06/07/2026]. See the Terms and Conditions (https://onlinelibrary.wiley.com/terms-and-conditions) on Wiley Online Library for rules of use; OA articles are governed by the applicable Creative Commons License

34. T. Clua-Provost, Z. Mu, A. Durand, et al., "Spin-Dependent Photodynamics of Boron-Vacancy Centers in Hexagonal Boron Nitride," *Physical Review B* 110 (2024): 014104.

35. W. Lee, V. S. Liu, Z. Zhang, et al., "Intrinsic High-Fidelity Spin Polarization of Charged Vacancies in Hexagonal Boron Nitride," *Physical Review Letters* 134 (2025): 096202.

36. J. R. Reimers, J. Shen, M. Kianinia, et al., "Photoluminescence, Photophysics, and Photochemistry of the V_B^- Defect in Hexagonal Boron Nitride," *Physical Review B* 102 (2020): 144105.

37. S. Baber, R. N. E. Malein, P. Khatri, et al., "Excited State Spectroscopy of Boron Vacancy Defects in Hexagonal Boron Nitride Using Time-Resolved Optically Detected Magnetic Resonance," *Nano Letters* 22, no. 1 (2021): 461–467.

38. B. Whitefield, M. Toth, I. Aharonovich, J. Tetienne, and M. Kianinia, "Magnetic Field Sensitivity Optimization of Negatively Charged Boron Vacancy Defects in hBN," *Advanced Quantum Technologies* (2023).

39. N. B. Manson, J. P. Harrison, and M. J. Sellars, "Nitrogen-Vacancy Center in Diamond: Model of the Electronic Structure and Associated Dynamics," *Physical Review B* 74, no. 10 (2006): 104303.

40. L. Robledo, H. Bernien, T. V. D. Sar, and R. Hanson, "Spin Dynamics in the Optical Cycle of Single Nitrogen-Vacancy Centres in Diamond," *New Journal of Physics* 13, no. 2 (2011): 025013.

41. F. Libbi, P. M. M. C. de Melo, Z. Zanolli, M. J. Verstraete, and N. Marzari, "Phonon-Assisted Luminescence in Defect Centers from Many-Body Perturbation Theory," *Physical Review Letters* 128 (2022): 167401.

42. M. Abdi, J.-P. Chou, A. Gali, and M. B. Plenio, "Color Centers in Hexagonal Boron Nitride Monolayers: A Group Theory and Ab Initio Analysis," *ACS Photonics* 5, no. 5 (2018): 1967.

43. V. Ivády, G. Barcza, G. Thiering, et al., "Ab Initio Theory of the Negatively Charged Boron Vacancy Qubit in Hexagonal Boron Nitride," *npj Computational Materials* 6, no. 1 (2020): 1.

44. D. Aude Craik, P. Kehayias, A. Greenspon, et al., "Microwave-Assisted Spectroscopy Technique for Studying Charge State in Nitrogen-Vacancy Ensembles in Diamond," *Physical Review Applied* 14 (2020): 014009.

45. F. Jules, M. M. Glazov, S. Roux, et al., "Non-Radiative Energy Transfer between Boron Vacancies in Hexagonal Boron Nitride and Other 2D Materials," 2025. https://arxiv.org/abs/2512.03970.

46. T. Clua-Provost, A. Durand, J. Fraunié, et al., "Impact of Thickness-Dependent Nanophotonic Effects on the Optical Response of Color Centers in Hexagonal Boron Nitride," *Nano Letters* (2024): 12915–12920.

47. W. Liu, N.-J. Guo, S. Yu, et al., "Spin-Active Defects in Hexagonal Boron Nitride," *Materials for Quantum Technology* 2, no. 3 (2022): 032002.

48. A. Gottscholl, M. Diez, V. Soltamov, et al., "Room Temperature Coherent Control of Spin Defects in Hexagonal Boron Nitride," *Science Advances* 7, no. 14 (2021): eabf3630.

49. S. L. Bayliss, D. W. Laorenza, P. J. Mintun, et al., "Optically Addressable Molecular Spins for Quantum Information Processing," *Science* 370, no. 6522 (2020): 1309.

50. M. D. Mckay, R. J. Beckman, and W. J. Conover, "A Comparison of Three Methods for Selecting Values of Input Variables in the Analysis of Output from a Computer Code," *Technometrics* 42, no. 1 (2000): 55.

51. S. K. Mann, A. Cowley-Semple, E. Bryan, et al., "Chemically Tuning Room Temperature Pulsed Optically Detected Magnetic Resonance," *Journal of the American Chemical Society* 147, no. 26 (2025): 22911.

52. C. F. J. Wu, "Jackknife, Bootstrap and Other Resampling Methods in Regression Analysis," *The Annals of Statistics* 14, no. 4 (1986): 1261.

53. Y. Dumeige, J.-F. Roch, F. Bretenaker, et al., "Infrared Laser Threshold Magnetometry with a NV Doped Diamond Intracavity Etalon," *Optics Express* 27, no. 2 (2019): 1706.

54. N. Aslam, G. Waldherr, P. Neumann, F. Jelezko, and J. Wrachtrup, "Photo-Induced Ionization Dynamics of the Nitrogen Vacancy Defect in Diamond Investigated by Single-Shot Charge State Detection," *New Journal of Physics* 15, no. 1 (2013): 013064.

55. S. M. Blakley, T. T. Mai, S. J. Moxim, et al., "Spectroscopy of Photoionization from the ^1E Singlet State in Nitrogen-Vacancy Centers in Diamond," *Physical Review B* 110 (2024): 134109.

56. K. V. Ung, C. A. Roncaioli, R. L. Walsworth, and S. M. Blakley, "High Resolution Temperature-Resolved Spectroscopy of the Nitrogen Vacancy ^1E Singlet State Ionization Energy," 2025, https://arxiv.org/abs/2507.10291.

57. W. Weston, D. Wickramaratne, M. Mackoit, A. Alkauskas, and C. G. Van de Walle, "Native Point Defects and Impurities in Hexagonal Boron Nitride," *Physical Review B* 97 (2018): 214104.

58. J. Strand, L. Larcher, and A. L. Shluger, "Properties of Intrinsic Point Defects and Dimers in Hexagonal Boron Nitride," *Journal of Physics: Condensed Matter* 32, no. 5 (2019): 055706.

59. A. Gali, "Recent Advances in the Ab Initio Theory of Solid-State Defect Qubits," *Nanophotonics* 12, no. 3 (2023): 359.

60. M. Hosseini, M. Arif, A. Keshavarz, and S. Iglauer, "Neutron Scattering: A Subsurface Application Review," *Earth-Science Reviews* 221 (2021): 103755.

61. J. R. Toledo and K. Krambrock, "Identification and Thermal Stability of Point Defects in Neutron-Irradiated Hexagonal Boron Nitride (h-BN)," *Journal of Physics D: Applied Physics* 54, no. 6 (2020): 065303.

Supporting Information

Additional supporting information can be found online in the Supporting Information section.

Supporting File: adom71351-sup-0001-SuppMat.pdf.

21951071, 2026, 25, Downloaded from https://advanced.onlinelibrary.wiley.com/doi/10.1002/adom.71351 by Andrew Beling - University Of Maryland , Wiley Online Library on [06/07/2026]. See the Terms and Conditions (https://onlinelibrary.wiley.com/terms-and-conditions) on Wiley Online Library for rules of use; OA articles are governed by the applicable Creative Commons License